Monthly Notices
of the
ROYAL ASTRONOMICAL SOCIETY

MNRAS **458,** 603–612 (2016)
Advance Access publication 2016 February 9

doi:10.1093/mnras/stw302

Digging deeper into the Southern skies: a compact Milky Way companion discovered in first-year Dark Energy Survey data

E. Luque,[1,2]★ A. Queiroz,[1,2] B. Santiago,[1,2]★ A. Pieres,[1,2] E. Balbinot,[2,3] K. Bechtol,[4] A. Drlica-Wagner,[5] A. Fausti Neto,[2] L. N. da Costa,[2,6] M. A. G. Maia,[2,6] B. Yanny,[5] T. Abbott,[7] S. Allam,[5] A. Benoit-Lévy,[8] E. Bertin,[9,10] D. Brooks,[8] E. Buckley-Geer,[5] D. L. Burke,[11,12] A. Carnero Rosell,[2,6] M. Carrasco Kind,[13,14] J. Carretero,[15,16] C. E. Cunha,[11] S. Desai,[17,18] H. T. Diehl,[5] J. P. Dietrich,[17,18] T. F. Eifler,[19,20] D. A. Finley,[5] B. Flaugher,[5] P. Fosalba,[15] J. Frieman,[5,21] D. W. Gerdes,[22] D. Gruen,[23,24] G. Gutierrez,[5] K. Honscheid,[25,26] D. J. James,[7] K. Kuehn,[27] N. Kuropatkin,[5] O. Lahav,[8] T. S. Li,[28] M. March,[19] J. L. Marshall,[28] P. Martini,[25,29] R. Miquel,[16,30] E. Neilsen,[5] R. C. Nichol,[31] B. Nord,[5] R. Ogando,[2,6] A. A. Plazas,[20] A. K. Romer,[32] A. Roodman,[11,12] E. Sanchez,[33] V. Scarpine,[5] M. Schubnell,[22] I. Sevilla-Noarbe,[13,33] R. C. Smith,[7] M. Soares-Santos,[5] F. Sobreira,[2,5] E. Suchyta,[25,26] M. E. C. Swanson,[14] G. Tarle,[22] J. Thaler,[34] D. Tucker,[5] A. R. Walker[7] and Y. Zhang[22]

Affiliations are listed at the end of the paper

Accepted 2016 February 5. Received 2016 February 5; in original form 2015 August 8

ABSTRACT

We use the first-year Dark Energy Survey (DES) data down to previously unprobed photometric depths to search for stellar systems in the Galactic halo, therefore complementing the previous analysis of the same data carried out by our group earlier this year. Our search is based on a matched filter algorithm that produces stellar density maps consistent with stellar population models of various ages, metallicities, and distances over the survey area. The most conspicuous density peaks in these maps have been identified automatically and ranked according to their significance and recurrence for different input models. We report the discovery of one additional stellar system besides those previously found by several authors using the same first-year DES data. The object is compact, and consistent with being dominated by an old and metal-poor population. DES 1 is found at high significance and appears in the DES images as a compact concentration of faint blue point sources. Assuming different spatial profile parameterizations, the best-fitting heliocentric distance and total absolute magnitude in the range of 77.6–87.1 kpc and $-3.00 \lesssim M_V \lesssim -2.21$, respectively. The half-light radius of this object, $r_h \sim 10$ pc and total luminosity are consistent with it being a low-mass halo cluster. It is also found to have a very elongated shape ($\epsilon \sim 0.57$). In addition, our deeper probe of DES first-year data confirms the recently reported satellite galaxy candidate Horologium II as a significant stellar overdensity. We also infer its structural properties and compare them to those reported in the literature.

Key words: globular clusters: general – globular clusters: individual (DES 1) – galaxies: dwarf.

1 INTRODUCTION

The census of Milky Way (MW) satellites has grown rapidly over the past 15 yr. Several of these newly found objects are star systems with very low luminosities ($-3.0 \lesssim M_V \lesssim 0$) and small half-light radii

★ E-mail: elmer.luque@ufrgs.br (EL); basilio.santiago@ufrgs.br (BS)

(<10 pc), being more consistent with star clusters (Koposov et al. 2007; Belokurov et al. 2010; Fadely et al. 2011; Muñoz et al. 2012; Balbinot et al. 2013). These clusters are thought to be suffering stellar mass-loss via dynamical processes such as tidal disruption or evaporation (Koposov et al. 2007; Kim & Jerjen 2015a). The number of dwarf galaxies around the MW has also increased significantly, from the 11 classical dwarfs known until the late 1990s, up to a total of 27 which were known by early this year (McConnachie 2012), thanks in large part to the Sloan Digital Sky Survey (SDSS). Several of the dwarfs found with SDSS are very low-luminosity systems with high M/L, thus representing some of the most dark matter rich objects (Simon & Geha 2007).

At the larger luminosities typical of globular clusters (GCs), $-10 \lesssim M_V \lesssim -5$ mag, different cluster sub-populations classified by their position, kinematics, and horizontal branch (HB) morphology have been known for several decades (Zinn 1985, 1993; Milone et al. 2014). The so-called young halo clusters may have originated in dwarf galaxies accreted by the MW (Zinn 1993; Lee, Demarque & Zinn 1994; Marino et al. 2014, 2015). Both types of objects seem to share a vast planar structure around the Galaxy, which also encloses several stellar and gaseous streams of clusters and dwarf galaxies (Pawlowski, Pflamm-Altenburg & Kroupa 2012; Pawlowski, McGaugh & Jerjen 2015). The accretion origin of part of the MW system of GCs is also supported by the fact that several of them are found to have positions and kinematics that relate them to the Sagittarius dwarf galaxy (Law & Majewski 2010). On the other hand, at the much lower luminosities ($M_V \geq -7.4$ mag) of the recent satellite discoveries, the very distinction between star clusters and dwarf satellites may become less clear, as attested by their respective loci in size and luminosity space. It is therefore important to pursue a complete census of faint stellar systems inhabiting the Galactic halo, and to characterize them in terms of structure, stellar populations, and dark matter content. Extrapolations of the SDSS results over the entire sky and over the currently known luminosity function of MW dwarfs indicate that this census is still very incomplete (Tollerud et al. 2008; Hargis, Willman & Peter 2014).

A very recent boost to the number of known MW satellites has been brought by the Dark Energy Survey (DES; Abbott et al. 2005). Using the first internal release of DES co-add data (Y1A1), Bechtol et al. (2015) reported on the discovery of eight new MW satellites over a solid angle of 1800 deg^2 in the southern equatorial hemisphere. Six of these systems have sizes and optical luminosities clearly consistent with the low-luminosity dwarfs previously detected in SDSS. The case for the other two objects is less clear. In a parallel effort, Koposov et al. (2015) reported nine new MW satellites using the same DES imaging data, including the same eight and one additional object. One of the objects in common between these two searches, Kim 2, had in fact been previously found by Kim et al. (2015) using data from the Stromlo MW Satellite Survey. In addition to that, Kim & Jerjen (2015b) have discovered yet another object using Y1A1 data, Horologium II. The Panoramic Survey Telescope and Rapid Response System 1 and the Survey of the Magellanic Stellar History have also been responsible for several recent discoveries of MW satellites (Laevens et al. 2014, 2015a,b; Martin et al. 2015).

As described in Bechtol et al. (2015), several complementary search strategies have been implemented within the DES Collaboration to search for stellar sub-structures. In Bechtol et al. (2015), we used a conservative star selection to ensure high stellar purity and completeness as well as a uniform field density over the survey footprint. The present work extends the results presented in Bechtol et al. (2015) by including stars at fainter magnitudes and by considering a broader range of spatial extensions as well as ages and metallicities for the stellar populations composing new satellite systems. We also describe in detail the application of another search algorithm to the Y1A1 co-add data. Together, these analysis updates have enabled the discovery of a new candidate stellar cluster, DES J0034−4902, which we call DES 1, and the confirmation of Horologium II as a physical stellar system. In Section 2, we describe the first-year DES data used. In Section 3, we describe the matched-filter (MF) algorithm applied to find the new systems. The new discovery is presented in Section 4. In Section 5, we report on the detection and characterization of Horologium II. Our final remarks are given in Section 6.

2 DES DATA

DES is a wide-field imaging programme expected to cover about 5000 deg^2 in the *grizY* bands down to $\simeq$ 24.6th magnitude (at S/N $\simeq$ 10 for galaxies in *g* band; Abbott et al. 2005) in the southern equatorial hemisphere for a period of five years. It uses the Dark Energy Camera (DECam), a 3 deg^2 (2.2 diameter) mosaic camera with 0.263 arcsec pixels on the prime focus of the Cerro Tololo Inter-American Observatory (CTIO) Blanco 4 m telescope (Flaugher et al. 2015). The DECam images are reduced by the DES Data Management (DESDM) team, which has developed a pipeline to process the data from basic single exposure instrumental corrections all the way to catalogue creation from calibrated co-added images. Here, we use the DES year one co-add catalogue data (Y1A1), taken from 2013 August to 2014 February. For more details on Y1A1 and DESDM, we refer to Sevilla et al. (2011), Mohr et al. (2012), and Gruendl et al., in preparation. The stellar sample used in this work was drawn using the SExtractor parameters `FLAGS`, `SPREAD_MODEL`, and point spread function (`PSF`) magnitudes (Bertin & Arnouts 1996; Desai et al. 2012; Bouy et al. 2013). We used a source quality criterion of `FLAGS` ≤ 3 over the *gri* filters. To avoid issues arising from fitting the `PSF` across variable-depth co-added images, we utilized the weighted-average (`WAVG`) of the `SPREAD_MODEL` measurements from the single-epoch exposures (for details, see Bechtol et al. 2015).

As mentioned above, Kim & Jerjen (2015b) have discovered one stellar object (Horologium II) in Y1A1 data that was not initially identified by Bechtol et al. (2015), or by Koposov et al. (2015). We believe that a primary reason for the non-detection of this object is that most of the probable member stars are fainter than $g \simeq 23$ mag, which is where Bechtol et al. (2015) set the faint-end threshold to search of stellar objects. This conservative threshold was set to ensure high stellar purity and completeness, as well as a uniform field density over the survey footprint.

In this work, we adopt a selection in `WAVG_SPREAD_MODEL` intended to increase stellar completeness relative to the analysis of Bechtol et al. (2015), specifically, *i*-band |`WAGV_SPREAD_MODEL`| < 0.003 + `WAVG_SPREADERR_MODEL`. A bright (faint) *g* magnitude limit of `WAVG_MAG_PSF` = 17 (`WAVG_MAG_PSF` = 24) was also applied. The faint limit is 1 mag deeper than used by Bechtol et al. (2015). In order to prevent point sources with extreme colours (including red dwarfs from the Galactic disc) from contaminating the sample, a colour cut at $-0.5 \leq g - r \leq 1.2$ was also used.

We estimated stellar completeness as follows. We first obtained a completeness curve that quantifies the stellar detection efficiency. This is determined by applying DAOPHOT to fields around DES 1 and Horologium II in the *g* and *r* filters. The fields selected are sub-regions of the co-added images encompassing

8.67 arcmin × 8.67 arcmin each. We then added sets of 450 artificial stars at a time, with 10 realizations for each filter from $\{g, r\} = 18$ mag down to 27 mag. These artificial stars were reduced in the same way as the real image, following the same IRAF tasks and PSF model. In addition, we have obtained a stellar completeness following the method described in Bechtol et al. (2015). This method basically quantifies the stellar classification efficiency. As in Bechtol et al. (2015), we have created a test sample of high stellar purity around from DES 1 and Horologium II using a colour-based selection ($r - i > 1.7$). We then applied the morphology-based star selection criteria (see above in the text) to evaluate the classification efficiency for the test sample. Our final stellar completeness was the product of the detection and classification efficiencies. The stellar completeness was found to be >90 per cent to $r \sim 23$ mag and falls to ∼80 per cent by $r \sim 24$ mag.

3 SEARCH METHOD

As discussed in Bechtol et al. (2015), several independent search methods were used in the original analysis of Y1A1 data. In this section, we describe in detail a different method, which was the one primarily used in this work.

3.1 Matched filter

The MF technique has several applications for signal processing. In the context of astronomy, it has been used to detect low-density features and populations in imaging data (Rockosi et al. 2002; Szabo et al. 2011). We here use it to search for new star clusters and dwarf galaxies following on the work by Balbinot et al. (2011).

The number of stars as a function of position on the sky (α,δ) and of colour (c) and magnitude (m) may be generally described as

$$n(\alpha, \delta, c, m) = n_{\rm cl}(\alpha, \delta, c, m) + n_{\rm bg}(\alpha, \delta, c, m). \quad (1)$$

The first term on the right-hand side corresponds to the contribution by the cluster (cl) we want to discover, whereas the second term represents the background (bg), which includes foreground halo stars and background unresolved galaxies. We then split these terms into a normalization term and a probability distribution function (PDF):

$$n_{\rm cl}(\alpha, \delta, c, m) = \zeta_{\rm cl}(\alpha, \delta) f_{\rm cl}(c, m), \quad (2)$$

where $\zeta_{\rm cl}$ and $f_{\rm cl}$ are the number normalization and PDF on the colour–magnitude diagram (CMD) plane, respectively, for the stellar population to be found. The stellar population may be extended in space (as in a stream), but we explicitly assume that its CMD is the same everywhere. As for the background stars, Galactic structure models show that both the number density and CMD vary as a function of position across the sky (Jurić et al. 2008). Therefore, we write

$$n_{\rm bg}(\alpha, \delta, c, m) = \zeta_{\rm bg}(\alpha, \delta) f_{\rm bg}(\alpha, \delta, c, m). \quad (3)$$

With the definitions above, equation (1) then becomes

$$n(\alpha, \delta, c, m) = \zeta_{\rm cl}(\alpha, \delta) f_{\rm cl}(c, m) + \zeta_{\rm bg}(\alpha, \delta) f_{\rm bg}(\alpha, \delta, c, m). \quad (4)$$

We bin stars into spatial pixels of area of 1.0 arcmin × 1.0 arcmin, indexed by i, and colour–magnitude bins of 0.01 mag × 0.05 mag, indexed by j. Details on the construction of the $f_{\rm cl}$ and $f_{\rm bg}$ PDFs are found in Section 3.2 and Section 3.3, respectively. With this notation,

$$n(i, j) = \zeta_{\rm cl}(i) f_{\rm cl}(j) + \zeta_{\rm bg}(i) f_{\rm bg}(i, j). \quad (5)$$

Table 1. Parameter grid used to simulate SSPs for the search of star systems in DES Y1 footprint.

Parameters	Lower limit	Upper limit	steps
log(Age)	9.0	10.2	0.3
Distance (kpc)	10	200	10
Metallicity, Z	0.0002, 0.001, and 0.007		

The left-hand side is the expected number of stars in a given spatial pixel and CMD bin. If the actual number of stars observed in a catalogue is $N(i, j)$, the variance between data and model is

$$s^2(i) = \sum_j \frac{[N(i, j) - \zeta_{\rm cl}(i) f_{\rm cl}(j) - \zeta_{\rm bg}(i) f_{\rm bg}(i, j)]^2}{\zeta_{\rm bg}(i) f_{\rm bg}(i, j)}. \quad (6)$$

The term in the denominator expresses the expected Poisson fluctuation in the star counts, which, for simplicity, we assume to be dominated by the background. Minimizing the variance and solving for $\zeta_{\rm cl}(i)$, we have the number of observed stars that, according to the model given by equation (4), are consistent with the model.

$$\zeta_{\rm cl}(i) = \frac{\sum_j N(i, j) f_{\rm cl}(j)/f_{\rm bg}(i, j)}{\sum_j f_{\rm cl}^2(j)/f_{\rm bg}(i, j)} - \frac{\zeta_{\rm bg}(i)}{\sum_j f_{\rm cl}^2(j)/f_{\rm bg}(i, j)}. \quad (7)$$

The output of the filter application is a stellar density map of stars which are probable cluster members stars, i.e. $\zeta_{\rm cl}(i)$. In practice, $f_{\rm bg}(i, j)$ is generated from our target stellar catalogue itself. We do that under the assumption that the contamination by any yet to be detected cluster, dwarf galaxy, or stellar stream, does not change the background PDF. As for the object PDF, we make use of simulated samples, as described in the next sub-section.

3.2 Model grid

Since we do not know a priori what stellar populations we will find, we create a grid of simple stellar populations (SSPs) with the code GENCMD.[1] GENCMD uses PARSEC isochrones by Bressan et al. (2012) for different assumed distances and randomly selects stellar masses following a predefined initial mass function (IMF). Currently, we are adopting a Kroupa (2001) IMF for that purpose. Given each stellar mass, we interpolate among the isochrone entries to draw absolute magnitudes in the desired filters. These are converted into *measured* apparent magnitudes using the assumed model distance, magnitude uncertainties taken from Y1A1, and the reddening map of Schlegel, Finkbeiner & Davis (1998). Positions on the sky may also be simulated assuming different profile models. We simulate several SSPs at various ages, metallicities and distances covering a broader range of isochrone choices, including younger and higher metallicity stellar populations, than those adopted in Bechtol et al. (2015). The parameter grid of these simulations is presented in Table 1.

3.3 Object detection

We apply the MF method as presented in Section 3.1 to the stellar catalogue using each of the SSPs in the model grid described in Section 3.2. In practice, the sky is partitioned into ∼10° × 10° cells to account for local variations in the background CMD, which is empirically derived from the stars in each individual cell. This

[1] https://github.com/balbinot/gencmd

procedure generates one density map for every sky cell and for every point in the model grid.

The maps are then convolved with Gaussian spatial kernels of different sizes $\{\sigma = 0.0$ arcmin (no convolution) to $\sigma = 9.0$ arcmin$\}$ to highlight sub-structure on scales typical of star clusters and ultrafaint dwarf galaxies. In particular, smaller spatial kernels are suitable for the detection of more compact stellar systems. Our range of spatial kernel sizes complements those adopted by Bechtol et al. (2015).

As it is not practical to visually inspect all the resulting maps from the large number of combinations of sky cells, SSP models, and spatial convolution kernels, we use the SExtractor code to automatically search for density peaks. In fact, the convolution kernels are applied from within SExtractor itself as we run it on maps of different sky regions resulting from different SSP models. Any object found by SExtractor in each map is recorded. Objects are then ranked according to the number of times they are detected by SExtractor. This is done separately for each sky cell and convolution kernel. The SExtractor parameters for the search were defined as those that maximized the recovery of simulated objects of different sizes and richness inserted into the DES stellar catalogue.

The first 10 objects in each region of the sky and for each convolution kernel are visually inspected to identify the most likely candidates. We visually checked the stellar density map around them, the Poisson statistical significance above the background represented by their associated stellar peak, their number density profile and CMD. The density maps, significance and density profiles provide a basic assessment of the overdensities being found. The CMD helps us judge if this overdensity is consistent with a stellar population. All these diagnostic tools are shown in the next section for DES 1.

We validated the detection method described above, which we call sparsex, by applying it to simulated SSPs superposed on real SDSS and DES data. We also tried to recover faint MW satellites previously discovered in SDSS data. In particular, we have chosen 17 objects found in SDSS data (11 dwarf galaxies and six star clusters) that are characterized as distant and ultrafaint objects. sparsex detected all these stellar objects at the top of the object ranking lists. The rate of success for simulated stellar systems with similar properties was the same. Finally, sparsex detected all eight satellites reported by Bechtol et al. (2015) and Horologium II reported by Kim & Jerjen (2015b). The latter is discussed in more detail in Section 5. The ninth object detected by Koposov et al. (2015) is in a region of Y1 data that is not included in the Y1A1 co-add due to limited coverage in some of the DES filters.

Table 2 lists the central position (α_0, δ_0), the peak Poisson significance and ranking position of objects detected by sparsex in Y1A1 data. The objects reported by Bechtol et al. (2015), Koposov et al. (2015), and Kim & Jerjen (2015b) are shown in the top nine lines in Table 2. DES 1 is also included. The Poisson significance profile is built by taking the ratio of the number of stars internal to each radius[2] r and in excess of the background ($N_{\rm bgd}$), $N_{\rm obj}$, to the expected fluctuation in the same background, i.e., $N_{\rm obj}/\sqrt{N_{\rm bgd}}$. $N_{\rm obj} = (N_{\rm obs} - N_{\rm bgd})$, where $N_{\rm obs}$ is the total number of observed stars. $N_{\rm bgd}$ is computed within an annulus at 30.0 arcmin $< r <$ 34.0 arcmin from each object. To avoid a low stellar statistic, we have built the Poisson significance profile using a cumulative radius of 1.0 arcmin centred on the object.

[2] For the initial sub-structure search, we evaluate the detection significance assuming circular symmetry.

Table 2. sparsex validation in Y1A1 data. Column 1: name of object. Column 2: right ascension. Column 3: declination. Column 4: ranking position. Column 5: peak Poisson significance.

Name	α_0 (deg)	δ_0 (deg)	Rank	Peak[a] significance
Ret II	53.92	−54.05	1.0	38.9
Eri II	56.09	−43.53	1.0	46.0
Tuc II	343.06	−58.57	1.0	9.1
Hor I	43.87	−54.11	1.0	24.1
Kim 2	317.20	−51.16	1.0	11.3
Pic I	70.95	−50.28	1.0	12.0
Phe II	354.99	−54.41	1.0	11.3
Eri III	35.69	−54.28	5.0	16.1
Hor II	49.12	−50.01	2.0	7.7
DES 1	8.50	−49.04	4.0	11.6

[a] Adopting a circular symmetry.

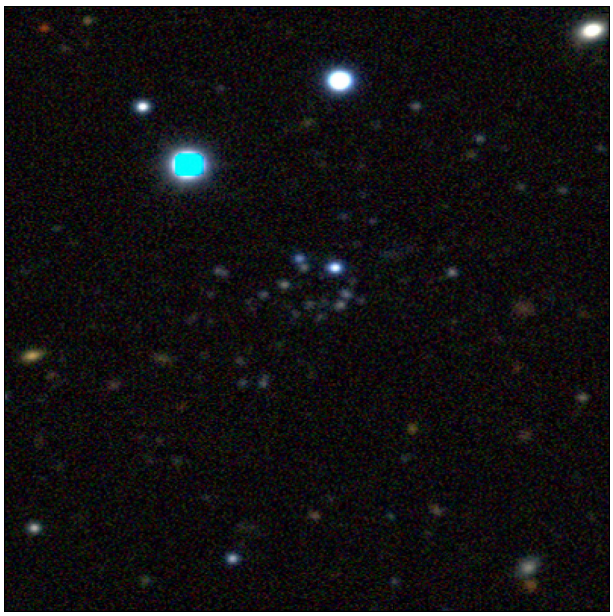

Figure 1. DES co-add image cutout of DES 1 taken from the DES Science portal. The image is 1.78 arcmin × 1.78 arcmin centred on DES 1. The R,G,B channels correspond to the i, r, g bands.

4 DES 1

DES 1 stands out as the most conspicuous new candidate from our search. It is also directly seen as an overdensity of blue stellar sources in the DES co-add images (Fig. 1). In Fig. 2, we show the number density of stars on the sky around this object (top panels). The left-hand panel shows all classified stellar sources, as described in Section 2, and the middle one shows only those close to the best-fitting isochrone (see Fig. 5 and associated discussion later in the text). A clear overdensity is seen in both. The elliptical Poisson significance profile[3] shows the higher peak at about 1.0 arcmin from the centre of DES 1 (see explanation in Section 3.3). This peak is clearly enhanced by filtering the stars according to our best-fitting

[3] The elliptical Poisson significance profile is built using the best-fitting structural parameters presented in this same section. Note that the semimajor axis of the ellipse, which we represent by the letter a, is equivalent to the elliptical radius defined in Martin, de Jong & Rix (2008).

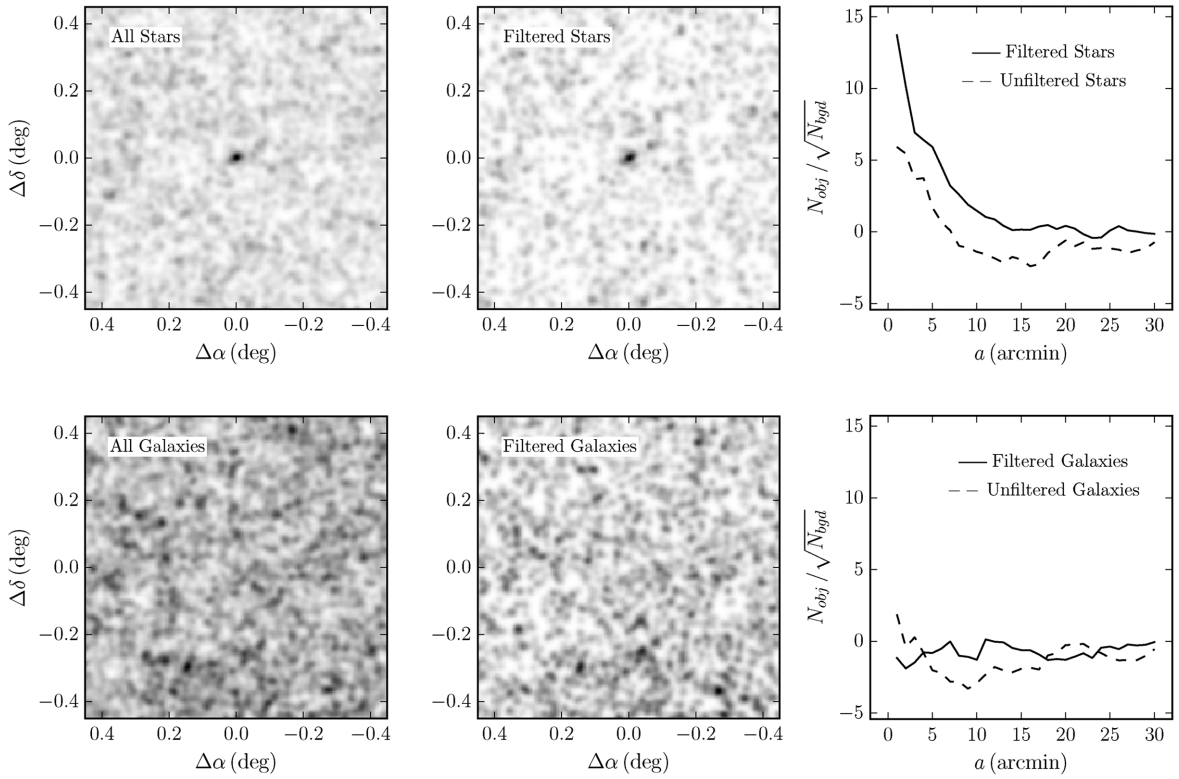

Figure 2. Top left panel: on-sky number density map of stellar sources around candidate DES 1. All stars are included. Top middle panel: similar to previous panel, but now only stars which lie close to the best-fitting isochrone shown in Fig. 5 are used. Density maps have been smoothed with a Gaussian kernel with standard deviation 0.′03. Top right panel: elliptical Poisson significance as a function of semimajor axis a from the centre of DES 1. The solid [dashed] line correspond to isochrone filtered [not pass the filter (unfiltered)] stars as indicated. The corresponding panels at the bottom show the same plots but using the distribution of sources classified as galaxies. *Note*. The centre was determined from the best-fitting exponential profile (see Table 3).

CMD model, discussed below. The bottom panels of Fig. 2 show that there is not an overdensity of galaxies at the position of DES 1, and therefore it is unlikely that misclassified galaxies can account for the apparent stellar overdensity.

We use a maximum-likelihood technique to infer structural and CMD parameters for DES 1. To estimate the structural properties for DES 1, we use two density profile models: exponential and empirical King (King 1962). The exponential profile has five free parameters: central RA (α_0) and Dec. (δ_0), position angle θ, ellipticity ϵ, and exponential scale r_e, whereas the King profile has six free parameters: α_0, δ_0, θ, ϵ, core radius r_c, and tidal radius r_t. We follow the same method as Martin et al. (2008) to find the best-fitting solution. For the parameter uncertainties, we follow a slight variant of Martin et al. (2008). The covariance between parameters is included in our uncertainty calculations via the profile likelihood technique (Sprott 2000, Section 4.5). We use 2σ (95.4 per cent confidence interval) to represent the structural and CMD parameter uncertainties.

The CMD fits weight each star by their membership probabilities p taken from the best profile fits. A threshold of $p \geq 1$ per cent is also adopted. We then use the CMDs of the most likely members of the system to fit an isochrone model, whose free parameters are: age, [Fe/H], $(m - M)_0$, and A_V. The method is based on finding the peak likelihood in a series of model grids, as described in detail by Pieres et al. (2015).

In Fig. 3, we show the results of the exponential profile fit to DES 1. The first three panels show the likelihood values projected on individual planes of this five-dimensional space, which all show well-defined peaks. The corresponding parameter values and their uncertainties (computed as discussed in Martin et al. 2008 and Pieres et al. 2015) are listed in Table 3. The last panel shows the individual stars coded by their membership probabilities. We note that DES 1 is a quite elongated object ($\epsilon \simeq 0.7$). Fig. 4 shows a binned density profile compared to the best-fitting exponential model. In both cases, we took into account the ellipticity. The central density of DES 1 is $\simeq 200$ stars arcmin^{-2}. A clear excess of stars relative to the background is seen out to $\simeq 2.0$ arcmin. In Fig. 4, we also show the best-fitting elliptical King profile. The set of structural parameters and their uncertainties determined by the maximum-likelihood fit are presented in Table 3. A visual inspection in Fig. 4 suggests that the King model best describes the central region and the excess stars seen out to $\simeq 2.0$ arcmin. We compute an estimate of half-mass radius[4] (r_h) for the King profile as follows. First, we have subtracted the expected number of field stars coinciding with DES 1, to obtain N_{DES1}, where N_{DES1} is the number of stars that belong to DES 1. We then compute r_h as the semimajor axis of the ellipse which contains $N_{DES1}/2$ stars (Balbinot et al. 2013). We obtain $r_h = 0.'39^{+0.13}_{-0.02}$ arcmin. The structural parameters determined by the exponential and King profiles agree within the uncertainties (see Table 3), confirming that DES 1 is a compact and quite elongated object.

The CMD for this candidate is shown on the left-hand panel of Fig. 5. Only stars inside an ellipse with semimajor axis $a = 2.0$ arcmin are shown. The middle panel shows the field

[4] To determine the half-mass radius, we have used the parameters determined from the best fit of King profile (see Table 3).

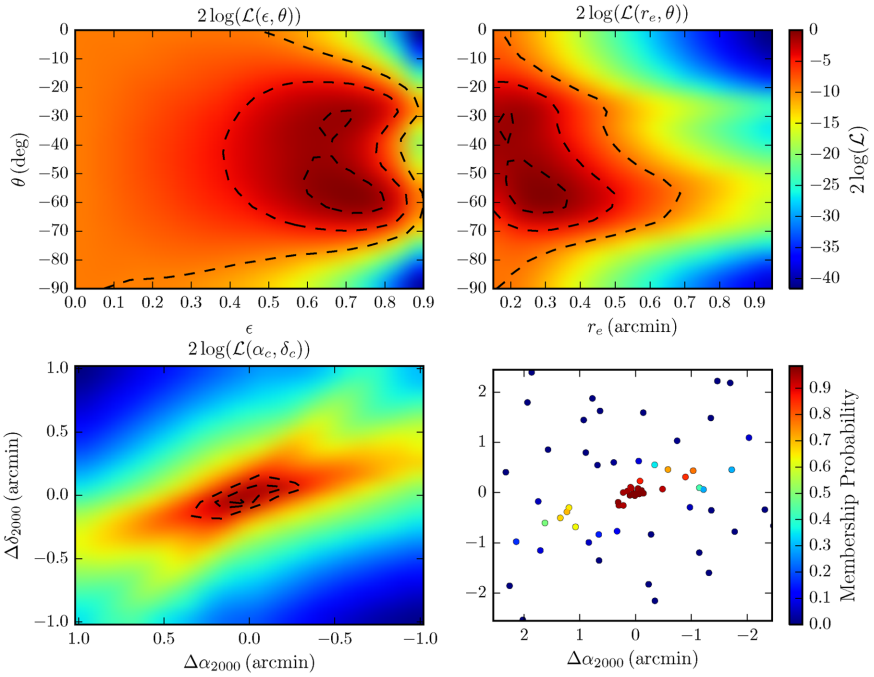

Figure 3. Upper left panel: likelihood map for DES 1 projected on to the position angle and eccentricity plane. Upper right: likelihood map for DES 1 projected on to the position angle and exponential scale plane. Lower left: likelihood map for DES 1 projected on to the central equatorial coordinates plane. The 1σ, 2σ and 3σ contour lines are shown. Lower right: spatial map of stars with probability larger than 1 per cent to belong to DES 1 colour-coded by probability. The best-fitting parameters are listed in Table 3.

Table 3. Properties of DES 1.

Parameters	Exponential profile	King profile
α_0 (J2000)	$00^h33^m59^s.7 \pm 9^s.4$	$00^h33^m59^s.6 \pm 1^s.4$
δ_0 (J2000)	$-49°02'20''.0 \pm 3''.6$	$-49°02'19''.8 \pm 2''.1$
$D_\odot$ (kpc)	∼87.1	∼77.6
r_e	$0'.23 \pm 0'.17$	–
θ (deg)	-57.9 ± 26.0	-52.5 ± 22.8
ϵ	0.69 ± 0.24	0.53 ± 0.22
Σ_c	204.98 ± 35.81	522.38 ± 88.30
Σ_{bgd}	2.02 ± 0.01	2.02 ± 0.01
r_h (arcmin)	0.39 ± 0.28^a	$0.39^{+0.13}_{-0.02}$
r_h (pc)	9.88 ± 7.09^b	$9.88^{+2.93}_{-0.45}{}^c$
M_V	$-3.00^{+0.66}_{-0.41}$	$-2.21^{+0.71}_{-0.48}$
TS	134.7	–
PS	13.7 ± 4.1	11.6 ± 3.9
r_c	–	$0'.08 \pm 0'.04$
r_t	–	$10'.75 \pm 5'.6$
[Fe/H][d]	-1.88 ± 0.25	-1.88 ± 0.05
log (Age)	10.00 ± 0.09	10.00 ± 0.06
A_V	0.0 ± 0.04	0.10 ± 0.07
$(m-M)_0$	19.70 ± 0.36	19.45 ± 0.11

[a]Using the relation, $r_h = 1.68 r_e$ (Martin et al. 2008).
[b]Adopting a distance of 87.1 kpc.
[c]Adopting a distance of 77.6 kpc.
[d]Adopting $Z_\odot = 0.0152$ (Bressan et al. 2012).
Note. Σ_c and Σ_{bgd} have units stars arcmin^{-2}.

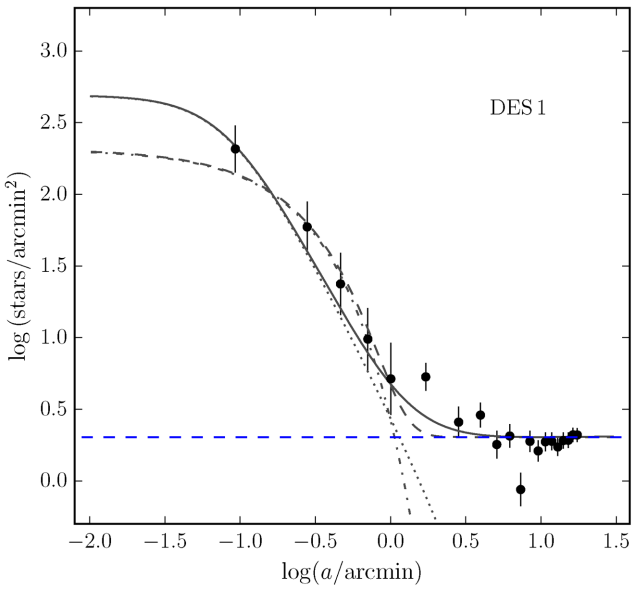

Figure 4. Solid points show a binned version of the density profile of DES 1, constructed in elliptical annuli using the derived structural parameters from the best-fit exponential profile (see Table 3). The error bars are 1σ Poisson uncertainties. Dot–dashed and dotted lines represent the best-fitting of exponential and King profiles, respectively. The horizontal dashed line shows the background level. Dashed and solid lines are the combination of the background level with the exponential and King profiles, respectively.

CMD in an elliptical annulus of equal area, whose inner semi-major axis is equal to 20.0 arcmin. The best-fitting isochrones derived from the likely members based on an exponential profile (solid line) and a King profile (dashed line) are also shown in Fig. 5; parameter values are listed in Table 3. Also shown are the sequences bracketing the best-fitting isochrone fit at a distance of $\sqrt{0.1^2 + \texttt{MAG\_ERR}^2 + \texttt{COL\_ERR}^2}$ on the CMD plane, where MAG_ERR and COL_ERR are the mean photometric uncertainties along the CMD axes. The 0.1 within the square root is a minimum isochrone mask width. It is meant to avoid

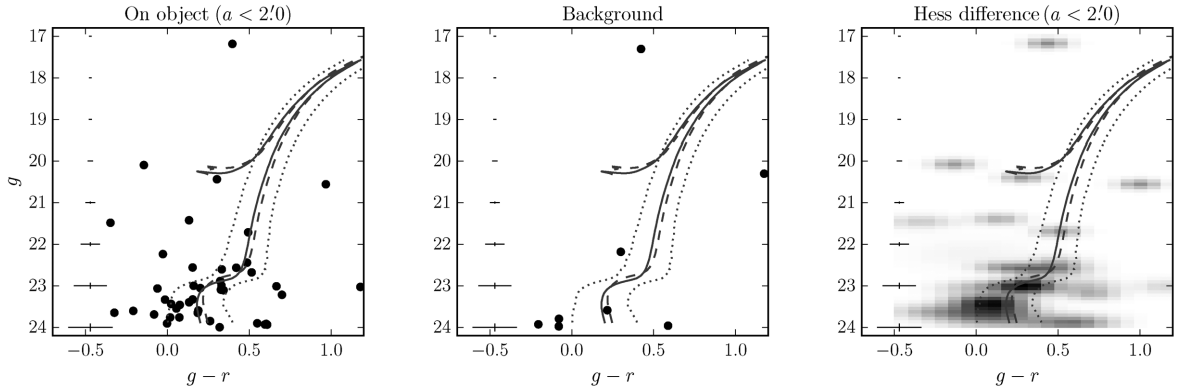

Figure 5. Left-hand panel: CMD of stars within an ellipse with semimajor axis $a = 2.0$ arcmin from the centre of DES 1. The best-fitting PARSEC isochrones (Bressan et al. 2012) are shown, along with ridge lines meant to bracket the most likely members. The best-fitting isochrone derived using the most likely stars as taken from an exponential profile is shown as a solid line, whereas the dashed line represents the best-fitting isochrone using the corresponding stars from a King profile. Middle panel: CMD of background stars in an elliptical annulus of equal area on the sky as the previous panel. Right-hand panel: Hess diagram of the CMD difference between stars within $a = 2.0$ arcmin and background stars (25.0 arcmin $< a <$ 40.0 arcmin). The mean photometric error is shown in the extreme left of each panel.

too narrow isochrone masks at the bright magnitudes, where uncertainties are small. We use the CMD space between them to filter the most likely cluster stars. See the middle and right-hand panels of Fig. 2 for a density map and an elliptical Poisson significance profile of objects inside this isochrone filter, respectively. The CMD difference relative to the background field, in their respective elliptical areas on the sky, is shown as the Hess diagram in the right-hand panel of Fig. 5. The main-sequence turn-off (MSTO) and sub-giant branch (SGB) are clearly visible.

As previously mentioned, we summarize the inferred properties of DES 1 in Table 3. The table lists positions, structural parameters, central (Σ_c) and background (Σ_{bgd}) densities, half-light radius (r_h), distance ($D_\odot$), absolute magnitude (M_V), test statistic (TS), peak Poisson significance (PS) value, core radius (r_c), and tidal radius (r_t), as well as best-fitting CMD parameters. The TS is based on the likelihood ratio between a hypothesis that includes an object versus a field-only hypothesis (see Bechtol et al. 2015).

In addition, we use Y2Q1[5] data to determine the properties of DES 1, but adopting a different magnitude threshold, $g < 23$ mag. By using a maximum-likelihood that simultaneously fits the profile (assuming a Plummer model) and the distance (but assuming an age of 12 Gyrs and a spread in metallicities), we obtain a distance modulus of $(m - M)_0 = 19.6$, in agreement with the method described earlier. The alternative r_h, however, is larger, $r_h \simeq 0.7$ arcmin. This value is marginally consistent with the previous ones reported here. Visual fits were also independently made to the object's CMD. Again, the results agree well with those from the maximum-likelihood fits shown on the table: log(Age) = 9.9, [Fe/H] = -1.88, $A_V = 0.03$, and $(m - M)_0 = 19.9$.

The quoted M_V estimate was computed by integrating overall masses along the best-fitting model isochrone assuming a Kroupa (2001) IMF, and normalizing the number of objects by those observed in the CMD with $r < 23$ mag and which fall in the isochrone filter. The star counts were corrected for sample incompleteness. As we count stars in $r < 23$ mag, the main source of uncertainty is due to small number of stars that are detected in the DES imaging.

[5] The Y2Q1 (year-two quick release) data set consists of exposures taken in the first and second years of DES. This data set is derived from single-epoch imaging instead (for details, see Drlica-Wagner et al. 2015).

We then calculate the uncertainty by estimating the upper and lower limits for the integrated V magnitude. We convert from DES g and r magnitudes to V magnitudes using

$$g_{SDSS} = g_{DES} + 0.104(g_{DES} - r_{DES}) - 0.01$$
$$r_{SDSS} = r_{DES} + 0.102(g_{DES} - r_{DES}) - 0.02$$
$$V = g_{SDSS} - 0.59(g_{SDSS} - r_{SDSS}) - 0.01. \quad (8)$$

This transform from DES g and r magnitudes to V-band magnitudes was derived using an SDSS stellar calibration sample and the equations from Jester et al. (2005) (see Bechtol et al. 2015).

5 HOROLOGIUM II

As mentioned earlier, Kim & Jerjen (2015b) report an additional MW satellite besides those found by Bechtol et al. (2015) and Koposov et al. (2015). Our reanalysis of Y1A1 presented here confirms this object, Horologium II, as a real stellar system. In fact, once we allow for a deeper magnitude threshold, as explained in Section 2, we detect it not only with the method described in Section 3 but also with the maximum-likelihood satellite search method described in Bechtol et al. (2015).

Fig. 6 shows the same information as Fig. 2, but now for Horologium II. A clear overdensity of stars is seen in the density map on the sky. The statistical significance of this overdensity is close to nine times the expected Poisson fluctuation in the background.

We have used the maximum-likelihood method to fit the spatial and CMD distributions as in the previous section. Table 4 lists the structural and isochrone parameters. The latter were derived from the most likely member stars when assuming an exponential profile.

The left-hand panel of Fig. 7 shows the CMD for Horologium II within an ellipse with semimajor axis $a = 3.0$ arcmin. The middle panel shows the background CMD in an elliptical annulus of equal area, whose inner semimajor axis is equal to 30.0 arcmin. The best-fitting PARSEC (Bressan et al. 2012) isochrone is shown. The sequences bracketing the best-fitting isochrone are also shown. The MSTO, SGB, and red giant branch are visible. Note that the CMD of Horologium II shows two stars that may belong to the HB. However, our maximum-likelihood fit assigns these stars a low probability of membership to Horologium II. The right-hand

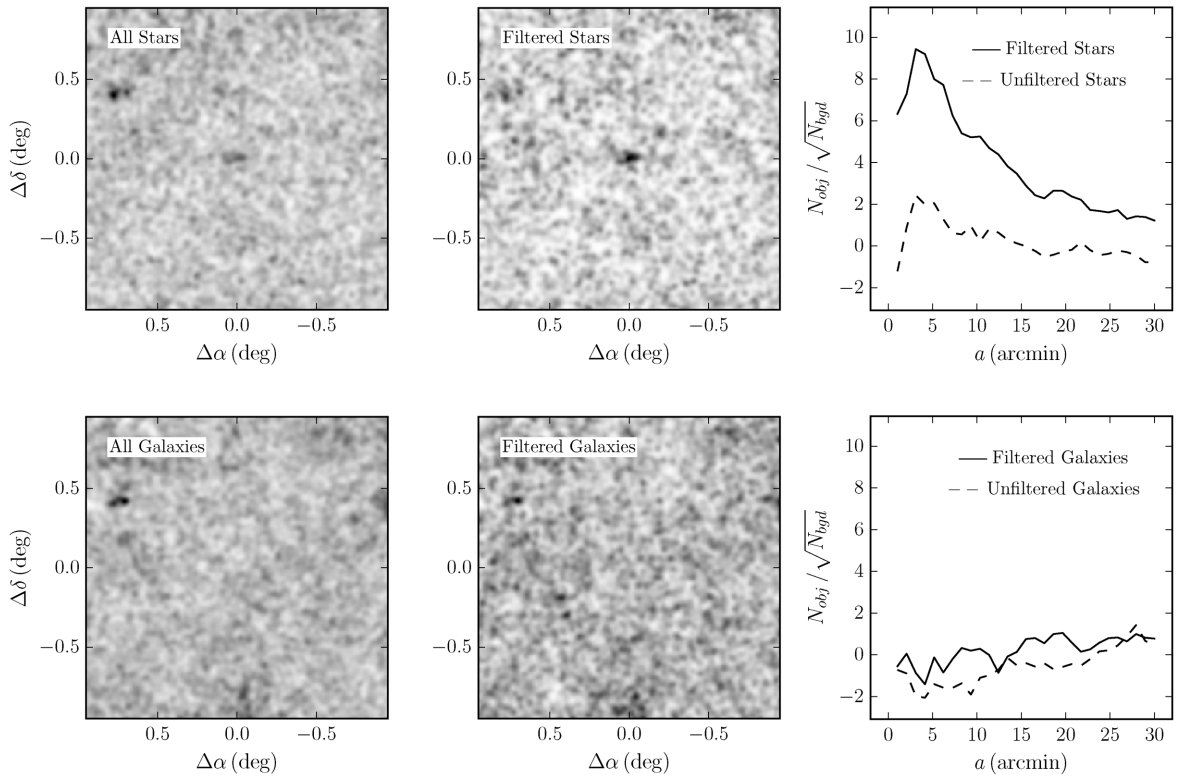

Figure 6. All panels are the same as those in Fig. 2 but now for the Horologium II satellite dwarf.

Table 4. Properties of Horologium II.

Parameters	Exponential profile
α_0 (J2000)	$03^h16^m27\overset{s}{.}6 \pm 39\overset{s}{.}3$
δ_0 (J2000)	$-50°00'36\overset{''}{.}7 \pm 46\overset{''}{.}7$
$D_\odot$ (kpc)	∼79.4
r_e	$1\overset{'}{.}32 \pm 0\overset{'}{.}45$
θ (deg)	106.3 ± 55.0
ϵ	0.57 ± 0.41
Σ_c (stars arcmin^{-2})	7.76 ± 1.29
Σ_{bgd} (stars arcmin^{-2})	1.80 ± 0.01
r_h	$2\overset{'}{.}22 \pm 0\overset{'}{.}76^a$
r_h (pc)	51.27 ± 17.55^b
M_V	$-2.72^{+0.67}_{-0.41}$
TS	52.3
PS	9.2 ± 2.7
[Fe/H]	-1.18 ± 0.24^c
log (Age)	9.88 ± 0.06
A_V	0.03 ± 0.11
$(m-M)_0$	19.50 ± 0.21

[a]Using the relation, $r_h = 1.68 r_e$ (Martin et al. 2008).
[b]Adopting a distance of 79.4 kpc.
[c]Adopting $Z_\odot = 0.0152$ (Bressan et al. 2012).

panel shows a binned elliptical density profile for Horologium II as a function of semimajor axis. For the centre of the overdensity, we adopt the value determined from the maximum-likelihood fit using an exponential profile. The best-fitting elliptical exponential profile is also overplotted.

Our distance, size, ellipticity, and absolute luminosity estimates are in good agreement (within 1σ) with those from the discovery paper by Kim & Jerjen (2015b). The position angle is within 2σ of its quoted value. The largest discrepancies occur for the isochrone parameters. We fit the observed CMD of Horologium II to a younger and more metal-rich PARSEC model than Kim & Jerjen (2015b). However, our likelihood function over the metallicity and age plane exhibits a tail of high-likelihood values towards lower Z and older ages. The discrepancy may also be related to the fact that our listed redenning value comes out of the maximum-likelihood CMD fit, whereas the values from Schlegel et al. (1998) maps (with corrections from Schlafly & Finkbeiner 2011) are used in the discovery paper.

6 CONCLUSIONS

In this paper, we make a deeper probe on the DES Y1A1 catalogue in search for additional Galactic satellites besides those previously reported by the collaboration (Bechtol et al. 2015). We report the discovery of a new stellar system in the MW halo, using catalogues based on first-year data from the DES. We have explored the data at least 1 mag deeper ($g < 24$ mag) than previously done in Bechtol et al. (2015). The candidate adds to the 11 previously identified systems found using DECam images (Bechtol et al. 2015; Kim & Jerjen 2015b; Kim et al. 2015; Koposov et al. 2015; Martin et al. 2015). We also confirm the dwarf galaxy candidate Horologium II, originally discovered by Kim & Jerjen (2015b), as a significant overdensity in the Y1A1 catalogue. Our best-fitting structural parameters for Horologium II are in general agreement with the ones derived by those authors, although the isochrone fit points to a younger and more metal-rich object than previously reported.

DES 1 is detected as a significant stellar overdensity both spatially and on the CMD plane. Isochrone fits based on two different methods show that it is made up of old and metal poor stars, as commonly observed in MW satellites found in the Galactic halo.

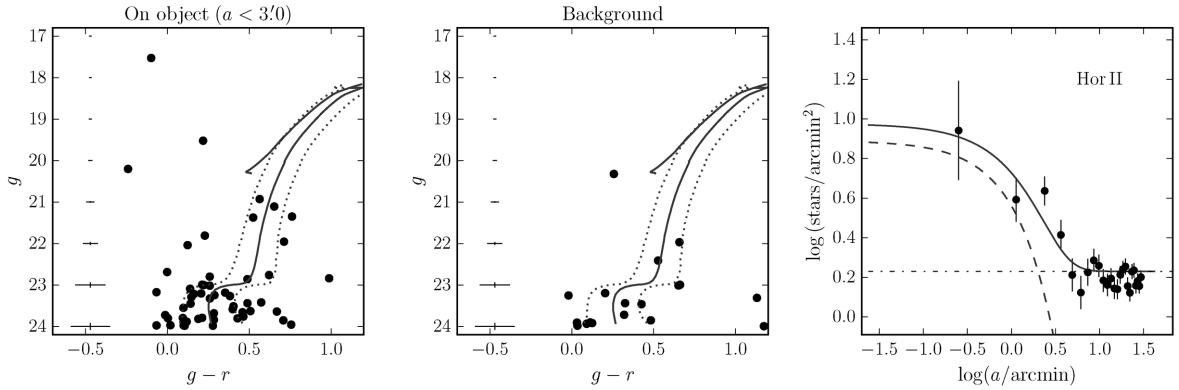

Figure 7. Left-hand panel: CMD of stars within an ellipse with semimajor axis $a = 3.0$ arcmin from the centre of Horologium II. The maximum-likelihood PARSEC (Bressan et al. 2012) isochrone fit is shown, along with ridge lines meant to bracket the most likely members. Middle panel: CMD of background stars in an elliptical annulus of equal area on the sky as the previous panel. The mean photometric error is shown in the extreme left of these panels. Right-hand panel: solid points show the binned density profile for Horologium II, constructed in elliptical annuli using the derived structural parameters from the best-fitting exponential profile (see Table 4). Error bars are based on a Poisson statistics. The dashed line shows the best fit of exponential profile, the horizontal dot–dashed line shows the background level, and the solid line represents the combination of both.

Maximum-likelihood fits of the King profile from DES 1 yield a core radius of $r_c \simeq 0.08$ arcmin, which at a distance $\simeq 77.6$ kpc corresponds to a physical size of $r_h \simeq 9.88$ pc. Its estimated distance places this faint cluster candidate as one of farthest away from the Sun. The absolute magnitude has been determined using a similar approach as Koposov et al. (2015), yielding $M_V \simeq -2.21$ for DES 1. Taken together, the physical size and luminosity place DES 1 in the locus occupied by low-luminosity star clusters. DES 1 is also significantly elongated [$\epsilon \simeq 0.69$ (Exponential), $\epsilon \simeq 0.53$ (King)], something that is apparent not only from the both profiles fit, but also from the distribution of the stars on the sky (Figs 1 and 3). It is, in fact, the most elongated halo cluster known to date, although, given the error bars, its ellipticity is marginally consistent with those of Kim 1, Laevens 3 (see Kim & Jerjen 2015a; Laevens et al. 2015b, respectively). The very high inferred ellipticity suggests that DES 1 is in dynamical process of tidal disruption, despite its large distance, and makes it a very interesting object for deeper imaging and spectroscopic follow up.

Due to the low number of probable member stars detected in the DES imaging, it is difficult to extract more reliable information about DES 1 at this stage. Steps to acquire deeper imaging of this object are already under way.

A search for satellites in data collected by the DES during its second season, including new areas sky, is under way. It is likely that additional new stellar systems will be discovered soon.

ACKNOWLEDGEMENTS

This paper has gone through internal review by the DES collaboration.

Funding for the DES Projects has been provided by the US Department of Energy, the US National Science Foundation, the Ministry of Science and Education of Spain, the Science and Technology Facilities Council of the United Kingdom, the Higher Education Funding Council for England, the National Center for Supercomputing Applications at the University of Illinois at Urbana-Champaign, the Kavli Institute of Cosmological Physics at the University of Chicago, the Center for Cosmology and Astro-Particle Physics at the Ohio State University, the Mitchell Institute for Fundamental Physics and Astronomy at Texas A&M University, Financiadora de Estudos e Projetos, Fundação Carlos Chagas Filho de Amparo à Pesquisa do Estado do Rio de Janeiro, Conselho Nacional de Desenvolvimento Científico e Tecnológico and the Ministério da Ciência, Tecnologia e Inovação, the Deutsche Forschungsgemeinschaft and the Collaborating Institutions in the DES. The DESDM system is supported by the National Science Foundation under Grant Number AST-1138766. The DES participants from Spanish institutions are partially supported by MINECO under grants AYA2012-39559, ESP2013-48274, FPA2013-47986, and Centro de Excelencia Severo Ochoa SEV-2012-0234, some of which include ERDF funds from the European Union.

The Collaborating Institutions are Argonne National Laboratory, the University of California at Santa Cruz, the University of Cambridge, Centro de Investigaciones Enérgeticas, Medioambientales y Tecnológicas-Madrid, the University of Chicago, University College London, the DES-Brazil Consortium, the University of Edinburgh, the Eidgenössische Technische Hochschule (ETH) Zürich, Fermi National Accelerator Laboratory, the University of Illinois at Urbana-Champaign, the Institut de Ciències de l'Espai (IEEC/CSIC), the Institut de Física d'Altes Energies, Lawrence Berkeley National Laboratory, the Ludwig-Maximilians Universität München and the associated Excellence Cluster Universe, the University of Michigan, the National Optical Astronomy Observatory, the University of Nottingham, The Ohio State University, the University of Pennsylvania, the University of Portsmouth, SLAC National Accelerator Laboratory, Stanford University, the University of Sussex, and Texas A&M University.

The DES data management system is supported by the National Science Foundation under Grant Number AST-1138766. The DES participants from Spanish institutions are partially supported by MINECO under grants AYA2012-39559, ESP2013-48274, FPA2013-47986, and Centro de Excelencia Severo Ochoa SEV-2012-0234.

Research leading to these results has received funding from the European Research Council under the European Union's Seventh Framework Programme (FP7/2007-2013) including ERC grant agreements 240672, 291329, and 306478.

EB acknowledges financial support from the European Research Council (ERC-StG-335936, CLUSTERS).

REFERENCES

Abbott T. et al., 2005, (arXiv:Astrophysics:e-prints)
Balbinot E., Santiago B. X., da Costa L. N., Makler M., Maia M. A. G., 2011, MNRAS, 416, 393
Balbinot E. et al., 2013, ApJ, 767, 101
Bechtol K. et al., 2015, ApJ, 807, 50
Belokurov V. et al., 2010, ApJ, 712, L103
Bertin E., Arnouts S., 1996, A&AS, 117, 393
Bouy H., Bertin E., Moraux E., Cuillandre J.-C., Bouvier J., Barrado D., Solano E., Bayo A., 2013, A&A, 554, A101
Bressan A., Marigo P., Girardi L., Salasnich B., Dal Cero C., Rubele S., Nanni A., 2012, MNRAS, 427, 127
Desai S. et al., 2012, ApJ, 757, 83
Drlica-Wagner A. et al., 2015, ApJ, 813, 109
Fadely R., Willman B., Geha M., Walsh S., Muñoz R. R., Jerjen H., Vargas L. C., Da Costa G. S., 2011, AJ, 142, 88
Flaugher B. et al., 2015, AJ, 150, 150
Hargis J. R., Willman B., Peter A. H. G., 2014, ApJ, 795, L13
Jester S. et al., 2005, AJ, 130, 873
Jurić M. et al., 2008, ApJ, 673, 864
Kim D., Jerjen H., 2015a, ApJ, 799, 73
Kim D., Jerjen H., 2015b, ApJ, 808, L39
Kim D., Jerjen H., Milone A. P., Mackey D., Da Costa G. S., 2015, ApJ, 803, 63
King I., 1962, AJ, 67, 471
Koposov S. et al., 2007, ApJ, 669, 337
Koposov S. E., Belokurov V., Torrealba G., Evans N. W., 2015, ApJ, 805, 130
Kroupa P., 2001, MNRAS, 322, 231
Laevens B. P. M. et al., 2014, ApJ, 786, L3
Laevens B. P. M. et al., 2015a, ApJ, 802, L18
Laevens B. P. M. et al., 2015b, ApJ, 813, 44
Law D. R., Majewski S. R., 2010, ApJ, 718, 1128
Lee Y.-W., Demarque P., Zinn R., 1994, ApJ, 423, 248
McConnachie A. W., 2012, AJ, 144, 4
Marino A. F. et al., 2014, MNRAS, 442, 3044
Marino A. F. et al., 2015, MNRAS, 450, 815
Martin N. F., de Jong J. T. A., Rix H.-W., 2008, ApJ, 684, 1075
Martin N. F. et al., 2015, ApJ, 804, L5
Milone A. P. et al., 2014, ApJ, 785, 21
Mohr J. J. et al., 2012, in Radziwill N. M., Chiozzi G., eds, Proc. SPIE Conf. Ser. Vol. 8451, Software and Cyberinfrastructure for Astronomy II. SPIE, Bellingham, p. 84510D
Muñoz R. R., Geha M., Côté P., Vargas L. C., Santana F. A., Stetson P., Simon J. D., Djorgovski S. G., 2012, ApJ, 753, L15
Pawlowski M. S., Pflamm-Altenburg J., Kroupa P., 2012, MNRAS, 423, 1109
Pawlowski M. S., McGaugh S. S., Jerjen H., 2015, MNRAS, 453, 1047
Pieres A. et al., 2015, preprint (arXiv:1512.01032)
Rockosi C. M. et al., 2002, AJ, 124, 349
Schlafly E. F., Finkbeiner D. P., 2011, ApJ, 737, 103
Schlegel D. J., Finkbeiner D. P., Davis M., 1998, ApJ, 500, 525
Sevilla I. et al., 2011, preprint (arXiv:1109.6741)
Simon J. D., Geha M., 2007, ApJ, 670, 313
Sprott D. A., 2000, Statistical Inference in Science. Springer-Verlag, Berlin
Szabo T., Pierpaoli E., Dong F., Pipino A., Gunn J., 2011, ApJ, 736, 21
Tollerud E. J., Bullock J. S., Strigari L. E., Willman B., 2008, ApJ, 688, 277
Zinn R., 1985, ApJ, 293, 424
Zinn R., 1993, in Smith G. H., Brodie J. P., eds, ASP Conf. Ser. Vol. 48, The Globular Cluster-Galaxy Connection. Astron. Soc. Pac., San Francisco, p. 38

[1]*Instituto de Física, UFRGS, Caixa Postal 15051, Porto Alegre, RS 91501-970, Brazil*
[2]*Laboratório Interinstitucional de e-Astronomia – LIneA, Rua Gal. José Cristino 77, Rio de Janeiro, RJ 20921-400, Brazil*
[3]*Department of Physics, University of Surrey, Guildford GU2 7XH, UK*
[4]*Kavli Institute for Cosmological Physics, University of Chicago, Chicago, IL 60637, USA*
[5]*Fermi National Accelerator Laboratory, PO Box 500, Batavia, IL 60510, USA*
[6]*Observatório Nacional, Rua Gal. José Cristino 77, Rio de Janeiro, RJ 20921-400, Brazil*
[7]*Cerro Tololo Inter-American Observatory, National Optical Astronomy Observatory, Casilla 603, La Serena, Chile*
[8]*Department of Physics and Astronomy, University College London, Gower Street, London WC1E 6BT, UK*
[9]*CNRS, UMR 7095, Institut d'Astrophysique de Paris, F-75014 Paris, France*
[10]*Sorbonne Universités, UPMC Univ Paris 06, UMR 7095, Institut d'Astrophysique de Paris, F-75014, Paris, France*
[11]*Kavli Institute for Particle Astrophysics & Cosmology, PO Box 2450, Stanford University, Stanford, CA 94305, USA*
[12]*SLAC National Accelerator Laboratory, Menlo Park, CA 94025, USA*
[13]*Department of Astronomy, University of Illinois, 1002 W. Green Street, Urbana, IL 61801, USA*
[14]*National Center for Supercomputing Applications, 1205 West Clark St, Urbana, IL 61801, USA*
[15]*Institut de Ciéncies de l'Espai, IEEC-CSIC, Campus UAB, Carrer de Can Magrans, s/n, E-08193 Bellaterra, Barcelona, Spain*
[16]*Institut de Física d'Altes Energies, Universitat Autònoma de Barcelona, E-08193 Bellaterra, Barcelona, Spain*
[17]*Excellence Cluster Universe, Boltzmannstr. 2, D-85748 Garching, Germany*
[18]*Faculty of Physics, Ludwig-Maximilians University, Scheinerstr. 1, D-81679 Munich, Germany*
[19]*Department of Physics and Astronomy, University of Pennsylvania, Philadelphia, PA 19104, USA*
[20]*Jet Propulsion Laboratory, California Institute of Technology, 4800 Oak Grove Dr., Pasadena, CA 91109, USA*
[21]*Kavli Institute for Cosmological Physics, University of Chicago, Chicago, IL 60637, USA*
[22]*Department of Physics, University of Michigan, Ann Arbor, MI 48109, USA*
[23]*Max Planck Institute for Extraterrestrial Physics, Giessenbachstrasse, D-85748 Garching, Germany*
[24]*Universitäts-Sternwarte, Fakultät für Physik, Ludwig-Maximilians Universität München, Scheinerstr. 1, D-81679 München, Germany*
[25]*Center for Cosmology and Astro-Particle Physics, The Ohio State University, Columbus, OH 43210, USA*
[26]*Department of Physics, The Ohio State University, Columbus, OH 43210, USA*
[27]*Australian Astronomical Observatory, North Ryde, NSW 2113, Australia*
[28]*George P. and Cynthia Woods Mitchell Institute for Fundamental Physics and Astronomy, and Department of Physics and Astronomy, Texas A&M University, College Station, TX 77843, USA*
[29]*Department of Astronomy, The Ohio State University, Columbus, OH 43210, USA*
[30]*Institució Catalana de Recerca i Estudis Avançats, E-08010 Barcelona, Spain*
[31]*Institute of Cosmology and Gravitation, University of Portsmouth, Portsmouth PO1 3FX, UK*
[32]*Department of Physics and Astronomy, Pevensey Building, University of Sussex, Brighton BN1 9QH, UK*
[33]*Centro de Investigaciones Energéticas, Medioambientales y Tecnológicas (CIEMAT), Madrid, Spain*
[34]*Department of Physics, University of Illinois, 1110 W. Green St, Urbana, IL 61801, USA*

This paper has been typeset from a TEX/LATEX file prepared by the author.